
Small-Animal PET/CT Assessment of Bone Microdamage in Ovariectomized Rats

Zhan-Chun Li, Sheng-Dan Jiang, Jun Yan, Lei-Sheng Jiang, and Li-Yang Dai

Department of Orthopaedic Surgery, Xinhua Hospital, Shanghai Jiaotong University School of Medicine, Shanghai, China

Microdamage in bone contributes to bone fragility in postmenopausal women. Therefore, it is important to find a noninvasive method to detect microdamage in living bone. PET with ^{18}F -fluoride has been used for skeletal imaging in clinical studies. However, few studies are undertaken to investigate bone microdamage associated with osteoporosis in vivo using noninvasive means. The aim of our study was to analyze the impact of osteoporosis due to estrogen deficiency on the occurrence of microdamage by observing the change in the uptake of ^{18}F -fluoride in the tibiae of ovariectomized rats after fatigue loading with small-animal PET/CT. We also explored the feasibility of noninvasive detection of bone microdamage in vivo using a small-animal PET/CT scanner specially designed for rodent study. **Methods:** Rats were randomized into 2 groups: ovariectomy and sham surgery. These rats were imaged using a dedicated small-animal PET scanner with ^{18}F -fluoride after the left tibiae were loaded cyclically under the axial compression. The fluoride uptake values were quantified in the tibial mid shafts, and the tibia was obtained for histomorphometric measurements of bone microdamage and osteocyte density. Bone mineral density at the fourth lumbar vertebra and right femur were measured using dual-energy x-ray absorptiometry. **Results:** PET image intensity was significantly increased ($P < 0.05$) in the loaded tibia of the ovariectomy group, compared with that of the sham group. Histomorphometry showed that both crack density and crack length in the loaded tibia were significantly higher ($P < 0.05$) in ovariectomized rats than in sham rats. The PET image intensity in the loaded tibia was significantly positively correlated with crack length and crack density (which show in histomorphometric measurement) ($P < 0.05$). **Conclusion:** Both small-animal PET/CT and histomorphometric measurement provided evidence that bone microdamage is significantly increased after estrogen depletion. The strong correlation between these 2 measurements suggests that small-animal PET/CT is a useful noninvasive means to detect bone microdamage in vivo.

Key Words: bone microdamage; osteoporosis; positron emission tomography; ^{18}F -fluoride; fatigue

J Nucl Med 2011; 52:769–775

DOI: 10.2967/jnumed.110.085456

As often defined by the decrease in bone strength and bone fractures subsequent to bone mass loss, osteoporosis has been more frequently linked with the deterioration of bone quality. Bone quality—more important than solely bone mass (1,2)—is now a widely embraced concept covering multiple aspects such as material composition and property, geometry, cellularity, bone turnover, mineralization, microarchitecture, and microdamage. Obviously, for screening and treating osteoporosis—and furthermore preventing and diagnosing osteoporotic fractures—more effective and precise imaging techniques are required because bone density, which is currently the most widely applied surrogate marker of bone strength and fracture risk, cannot in isolation fully explain bone strength.

Microdamage—closely related to the reconstruction process of the bone tissue—is microscopically detectable damage to the bone matrix. Cyclic mechanical loading may cause microdamage through the fatigue process, thereby impairing the mechanical integrity of bone by microdamage accumulation and even leading to a fracture (3–5). The repair of bone microdamage needs adaptive modeling and remodeling of bone to compensate for abnormalities through certain feedback mechanisms (6–8). The repair capacity may be impaired by age- and menopause-related abnormalities in bone remodeling (9–11). However, the relationship between osteoporosis and bone microdamage has not been fully addressed.

Recently, ^{18}F -fluoride with PET has been used for skeletal imaging in clinical studies (12–15). Because the increase of fluoride uptake is highly correlated with the increase of bone microdamage, it is possible to quantitatively and qualitatively evaluate bone microdamage noninvasively in vivo as the response to fatigue mechanical loading. The aim of our study was to analyze the impact of osteoporosis due to estrogen deficiency on the occurrence of microdamage by observing the change in ^{18}F -fluoride uptake in the tibia of ovariectomized rats after fatigue loading with small-animal PET/CT. We also explored the feasibility of noninvasive detection of bone microdamage in vivo using a small-animal PET/CT scanner specially designed for rodent study.

MATERIALS AND METHODS

Animals

Twenty-four female virgin Sprague–Dawley rats (age, 6 mo; weight, 290–310 g) were studied. These rats were randomized into

Received Nov. 18, 2010; revision accepted Jan. 31, 2011.
For correspondence or reprints contact: Li-Yang Dai, Department of Orthopaedic Surgery, Xinhua Hospital, 1665 Kongjiang Rd., Shanghai 200092, China.
E-mail: chinaspine@163.com
COPYRIGHT © 2011 by the Society of Nuclear Medicine, Inc.

2 groups ($n = 12$ in each group): ovariectomy and sham surgery. After being intraperitoneally anesthetized with pentobarbital (40 mg/kg), the rats in the ovariectomy group were bilaterally ovariectomized via back incisions, and fat tissue of the same weight as the excised ovaries was removed in the sham group. The animals were housed in individual cages in a temperature-controlled room at 22°C with a 12-h light–dark cycle and free access to food and distilled water. Body weight was measured once a week. The protocol of our study was approved by the Institutional Animal Care and Use Committee of Shanghai Jiaotong University, in accordance with the *Guide for the Care and Use of Laboratory Animals* (16).

Experimental Design

Twelve rats (6 rats in each group) were randomly allocated to receive fatigue loading in the left hind limbs 3 mo postoperatively. After loading for 10 d, the rats were sent for small-animal PET/CT evaluation and then sacrificed with exsanguinations from the abdominal aorta. Their fourth lumbar vertebrae and right femora and bilateral tibiae were harvested for further bone mineral density (BMD) and microdamage evaluation, respectively. In contrast to the left hind limbs, which were loaded cyclically under axial compression, the unloaded right hind limbs were used as the controls. The remaining 12 rats (6 rats in each group) did not undergo fatigue loading. The rats in this group were killed 3 mo after ovariectomy or sham surgery. Calcein was intraperitoneally injected 13 and 3 d before sacrifice, respectively. After the sacrifice, the right tibial shafts were harvested for histomorphometric measurement. The rats' uteri were also removed and weighed.

In Vivo External Mechanical Loading

Rats were anesthetized intraperitoneally with pentobarbital (40 mg/kg). Then they were placed prone on the loading platens of a mechanical testing machine (Instron 8874; Instron Limited) with the left knees flexed and the flexed knee and ankle joints placed in concaved cups, as described previously (15–18). Briefly, the upper and lower cups were attached to the actuator of the machine and the load cell, respectively. The position of the platens was adjusted to apply dynamic compressive loads axially to the tibia. With a preload of 0.5 N, dynamic compressive loads (peak loads of 48–52 N, 4 Hz, sinusoidal wave) were applied axially to the tibia. According to the results of our preliminary study, a peak load of 50 N engendered approximately 5,300 $\mu\epsilon$ and was sufficient to induce microdamage in the loaded tibia. After fatigue loading, intramuscular buprenorphine hydrochloride (0.05 mg/kg) was administered for pain relief (19). The load was applied 1,200 times per day for 5 d before a break of 2 d, and then continued for 5 d.

BMD Measurement

Because both previous study (20) and our preliminary experiment showed poor precision in BMD measurement of the tibia, the femur and spine were chosen as BMD measurement sites to facilitate experiments. BMD at the fourth lumbar vertebrae and right femora were determined in both groups by dual-energy x-ray absorptiometry on a Discovery-A (Hologic) system, using high-resolution BMD test software for small animals (Regional High Resolution, version 4076; Hologic). A region of interest was drawn, and the BMD of this region was calculated. The variation coefficient of inter- and intra-analyzer variations for BMD measurement was less than 2.0% in our laboratory.

Bone Histomorphometric Measurement

The right tibia was dehydrated in ethanol, embedded in polymethylmethacrylate, and sectioned with a Leica/Jung 2065 microtome without decalcification. The 50- μm -thick longitudinal sections from the proximal tibia were prepared for analysis of the geometric structure of the cancellous bone, and horizontal sections from the tibial mid shafts were prepared for analysis of histomorphometry of the cortical bone. Parameters for the geometric structure of the cortical bone included total tissue area (mm^2), cortical area (mm^2), percentage cortical area, medullary area (mm^2), and percentage medullary area, and variables for the cancellous bone included bone volume fraction (%), trabecular thickness (μm), trabecular number ($\#/\text{mm}^2$), and trabecular separation (μm). Parameters for bone formation included mineralizing surface (%), mineral apposition rate ($\mu\text{m}/\text{d}$), and bone formation rate ($\mu\text{m}^3/\mu\text{m}^2/\text{d}$). Measurement was made with the light microscope and fluorescence microscope (Axioplan 2 imaging; Carl Zeiss), using image analysis software KS400 (version 3.0 for Windows [Microsoft]; Zeiss). Nomenclature and units according to the recommendations of the Nomenclature Committee of the American Society for Bone and Mineral Research were adopted for all parameters for bone structure and bone formation in the study (21).

Small-Animal PET/CT Analysis

Rats in both groups were assessed by small-animal PET/CT on the day after fatigue loading using a small-animal PET/CT scanner (Inveon; Siemens Medical Solutions USA), with a 9.0-cm transverse field of view, a 5.8-cm axial field of view, and a spatial resolution of 2.58 mm. After 6 h of fasting, all of the rats were

TABLE 1
Bone Histomorphometric Parameters in Tibiae

Parameter	Sham	Ovariectomy
Geometric parameters		
Total tissue area (mm^2)	6.28 \pm 0.95	6.32 \pm 0.73
Cortical area (mm^2)	4.66 \pm 0.36	4.59 \pm 0.47
Percentage cortical area (%)	74.93 \pm 7.10	72.83 \pm 5.55
Medullary area (mm^2)	1.62 \pm 0.70	1.73 \pm 0.48
Percentage medullary area (%)	25.07 \pm 7.10	27.17 \pm 5.55
Microarchitectural parameters		
Bone volume fraction (%)	28.75 \pm 5.64	19.25 \pm 2.80*
Trabecular thickness (μm)	58.70 \pm 5.15	47.91 \pm 4.55*
Trabecular number ($\#/\text{mm}^2$)	4.42 \pm 0.36	3.35 \pm 0.26*
Trabecular separation (μm)	258.94 \pm 45.22	369.32 \pm 52.31*
Dynamic parameters		
Mineralizing surface (%)	6.12 \pm 1.22	7.97 \pm 1.25*
Mineral apposition rate ($\mu\text{m}/\text{d}$)	0.63 \pm 0.07	0.89 \pm 0.14*
Bone formation rate ($\mu\text{m}^3/\mu\text{m}^2/\text{d}$)	0.039 \pm 0.010	0.070 \pm 0.005*

Data are expressed as mean \pm SD.

* $P < 0.05$ vs. sham.

anesthetized with 2% isoflurane and injected with 44.4–62.9 MBq (1.2–1.7 mCi) of ^{18}F -NaF through the tail vein. Ten-minute CT scans were obtained with an x-ray tube voltage of 80 kV and a current of 500 μA to acquire the skeletal images at 48- μm resolution. Then, the skeleton was 3-dimensionally reconstructed using the acquired CT data in a real-time CT reconstruction system (COBRA_Exxim, version V3.0; Exxim Computing Corp.). PET was started at 1 h after injection of the radionuclide to acquire data regarding the uptake of ^{18}F -NaF. The data were acquired for 1 h. PET and CT images were fused automatically using the manufacturer's software (Inveon Acquisition Workplace 1.4; Siemens Medical Solutions USA, Inc.). Data regarding ^{18}F uptake were also recorded. With regions of interest drawn over the hind limbs, the normalized PET image intensity in the tibial mid shafts was defined as the ratio of PET image intensity of ^{18}F -fluoride in regions of interest of the hind limbs to intensity of muscles (22,23).

Microdamage Histomorphology Analysis

For the observation of microdamage, the tibia was bulk-stained with 1% basic fuchsin, as described previously (24,25). Briefly, after being stained in a graded series of ethanol (80%, 90%, and 100%), the isolated tibia was embedded in polymethylmethacrylate. Longitudinal 50- μm -thick sections without decalcification were made from the tibial shafts and examined for morphometric analysis of bone microdamage. The sections were first observed

using a fluorescence microscope (LSM510; Carl Zeiss). When microdamage, defined as a linear microcrack within the cortex, was detected, the areas containing microdamage were selectively examined using 2-photon confocal laser scanning microscopy (LSM510; Carl Zeiss). The measured histomorphometric variables included mean microcrack length (Cr.Le, μm), microcrack density (Cr.Dn, $\#/ \text{mm}^2$), microcrack surface density (Cr.S.Dn, $\mu\text{m}^2 / \text{mm}^2$), and osteocyte lacunar density (Ot.Dn, $\#/ \text{mm}^2$).

Statistical Analysis

Data are expressed as mean \pm SD. Comparison of results between the ovariectomy and sham groups was made by independent-samples *t* test. The results in both ovariectomy and sham groups are expressed as the difference (Δ) between the loaded and control limbs. When results between hind limbs within the same rats were compared, a paired *t* test was used. Pearson correlation was used to test the relationship between variables regarding PET intensity, BMD, and microdamage histomorphology. All statistical analyses were performed using SPSS 10.0 software (SPSS Inc.). A value of *P* less than 0.05 was considered statistically significant.

RESULTS

Validation of Model

Uterine and body weights at 3 mo after ovariectomy or sham surgery were compared. As expected, after ovariectomy,

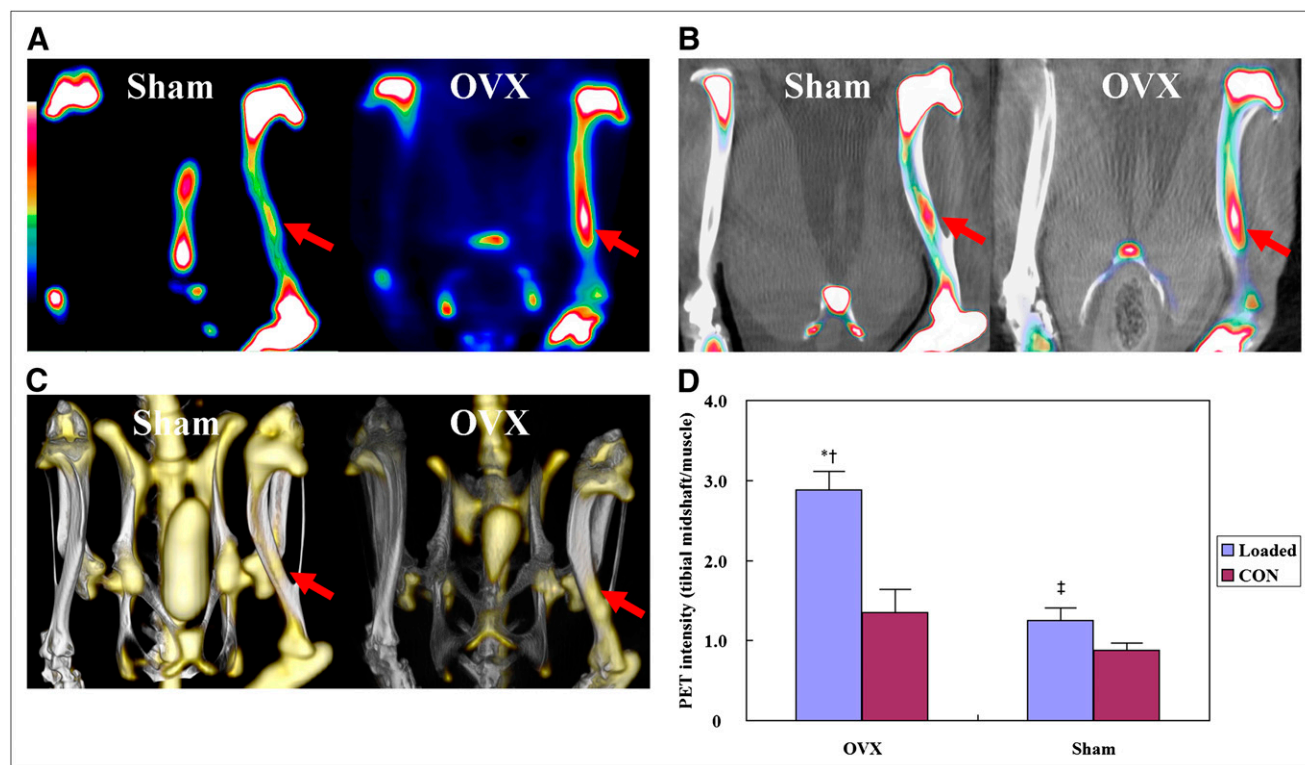


FIGURE 1. Small-animal PET/CT images of rat tibiae. (A) ^{18}F -fluoride PET image showing focally increased tracer uptake in mid shaft of loaded tibia. (B) Coregistered PET/CT coronal plane image. (C) Three-dimensionally reconstructed coregistered PET/CT image of rat tibia. In PET images, ^{18}F -fluoride is shown in proportion to color intensity. Increased intensity was observed in regions of trabecular bone (e.g., proximal tibia and vertebrae) because of bone surface area and higher bone turnover in these regions. Intensity was quantified in central region of left tibia (red arrow), and bone in region was exclusively cortical. Increased intensity was attributed solely to bone microdamage. (B and C) PET intensity in left tibia of ovariectomy group was higher than that of sham group. (D) PET intensity in loaded tibial mid shafts of ovariectomy group was significantly higher than that of sham group ($P < 0.05$). Data were expressed as mean \pm SD ($n = 6$ in each group). CON = control; OVX = ovariectomy. * $P < 0.05$, Δ PET intensity in ovariectomy vs. Δ PET intensity in sham. † $P < 0.05$ vs. ovariectomy plus control. ‡ $P < 0.05$ vs. sham plus control.

uterine wet weights were significantly reduced (0.162 ± 0.013 vs. 0.803 ± 0.077 g for ovariectomy vs. sham surgery, respectively; $P < 0.05$) and body weights were significantly increased (353 ± 6 vs. 334 ± 4 g for ovariectomy vs. sham surgery, respectively; $P < 0.05$). The results of bone histomorphometry are shown in Table 1. For the structural parameters of the cancellous bone, bone volume fraction, trabecular thickness, and trabecular number were significantly lower ($P < 0.05$) in the ovariectomy group than in the sham group, whereas trabecular separation was significantly higher ($P < 0.05$). With regard to dynamic parameters of the cancellous bone, mineralizing surface, mineral apposition rate, and bone formation rate in the ovariectomy group, compared with the sham group, were significantly increased ($P < 0.05$). However, there was no significant difference ($P > 0.05$) in the cortical bone parameters such as total tissue area, cortical area, percentage cortical area, medullary area, and percentage medullary area between the 2 groups.

Bone Microdamage as Shown by Small-Animal PET/CT

Significant increase in ^{18}F -fluoride uptake was shown in the central portion of the loaded hind limbs in both ovariectomy and sham rats, whereas no enhancement of ^{18}F -fluoride accumulation was seen in the unloaded hind limbs on small-animal PET/CT images (Figs. 1A–1C). The PET image intensity in the loaded tibial mid shafts of the ovariectomy group was significantly higher ($P < 0.05$) than that in the same region of the sham group (Fig. 1D).

Relationship Between PET Image Intensity and BMD or Microdamage Histomorphology

BMD at the fourth lumbar vertebrae and right femora of the ovariectomy group was significantly lower than that of the sham group (lumbar vertebrae, 0.235 ± 0.016 vs. 0.212 ± 0.018 g/cm²; femora, 0.261 ± 0.019 vs. 0.240 ± 0.013 g/cm²; $P < 0.05$) after being adjusted for the body weight. The PET image intensity in the loaded tibia was negatively correlated with BMD of either the femora or the lumbar spine ($P < 0.05$) (Supplemental Figs. 1A and 1B; supplemental materials are available online only at <http://jnm.snmjournals.org>).

Linear microcracks were shown on microscopy in all loaded tibiae of both ovariectomy and sham rats after axial fatigue loading (Fig. 2) but were not noted in any of the controlled tibiae of these rats. The Cr.Le, Cr.Dn, and Cr.S.Dn of the microcracks were significantly higher (Table 2) ($P < 0.05$) and Ot.Dn was significantly lower ($P < 0.05$) in the loaded tibia of the ovariectomy group than in the loaded tibia of the sham group (Supplemental Fig. 2). The PET image intensity in the loaded tibia was significantly positively ($P < 0.05$) correlated with Cr.Le, Cr.Dn, and Cr.S.Dn of the microcracks (Supplemental Figs. 1C–1E) and negatively ($P < 0.05$) correlated with Ot.Dn (Supplemental Fig. 1F).

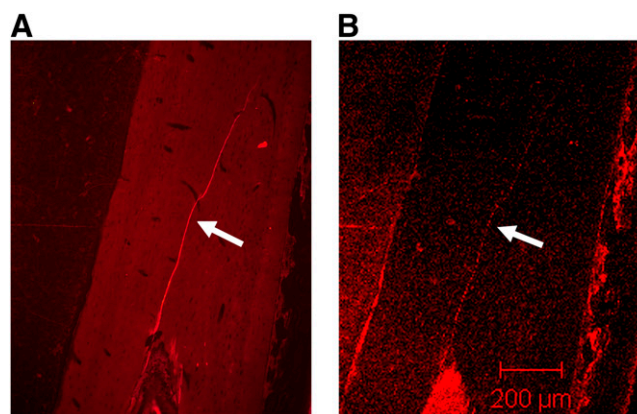


FIGURE 2. Longitudinal calcified section of fatigued rat tibial diaphysis, showing microcracks (magnification, $\times 100$). (A) Fluorescent microscopy of microcracks bulk-stained with fuchsin (arrow). (B) Laser confocal microscopy of microcracks bulk-stained with fuchsin (arrow). Scale bar = 200 μm .

Relationship Between Microdamage Histomorphology and BMD

Variables (Cr.Le, Cr.Dn, Cr.S.Dn, and Ot.Dn) correlated significantly ($P < 0.05$) with BMD at all measurement sites except between Cr.Le and lumbar BMD ($P > 0.05$) (Fig. 3).

DISCUSSION

It is generally believed that osteoporosis is associated with an increased risk of fracture. However, the relationship between osteoporosis and bone microdamage has not been fully addressed. Our current study showed that ovariectomy has led to more microdamage accumulation in bones loaded cyclically when evaluated by both in vivo and in vitro measurement. The magnitude of bone microdamage as shown by small-animal PET/CT and bone histology was negatively correlated with BMD. Until now, few studies have documented the impact of estrogen depletion or postmenopausal osteoporosis on bone microdamage accumulation. Dai et al. (26) found that more microdamage was noted in ovariectomized rats than in rats undergoing sham surgery and that microdamage accumulation was associated with a decrease of bone mass and biomechanical properties. They suggested that microdamage be used for bone-quality assessment in osteoporosis study. In a cross-sectional study

TABLE 2
Microdamage Histomorphologic Results in Tibiae

Parameters	Sham plus loaded	Ovariectomy plus loaded
Cr.Le (μm)	638.68 ± 413.10	$898.82 \pm 491.47^*$
Cr.Dn (number/mm ²)	1.20 ± 0.62	$1.99 \pm 0.51^*$
Cr.S.Dn ($\mu\text{m}/\text{mm}^2$)	748.82 ± 391.35	$1,703.41 \pm 702.12^*$

Data are expressed as mean \pm SD.

* $P < 0.05$ vs. sham plus loaded.

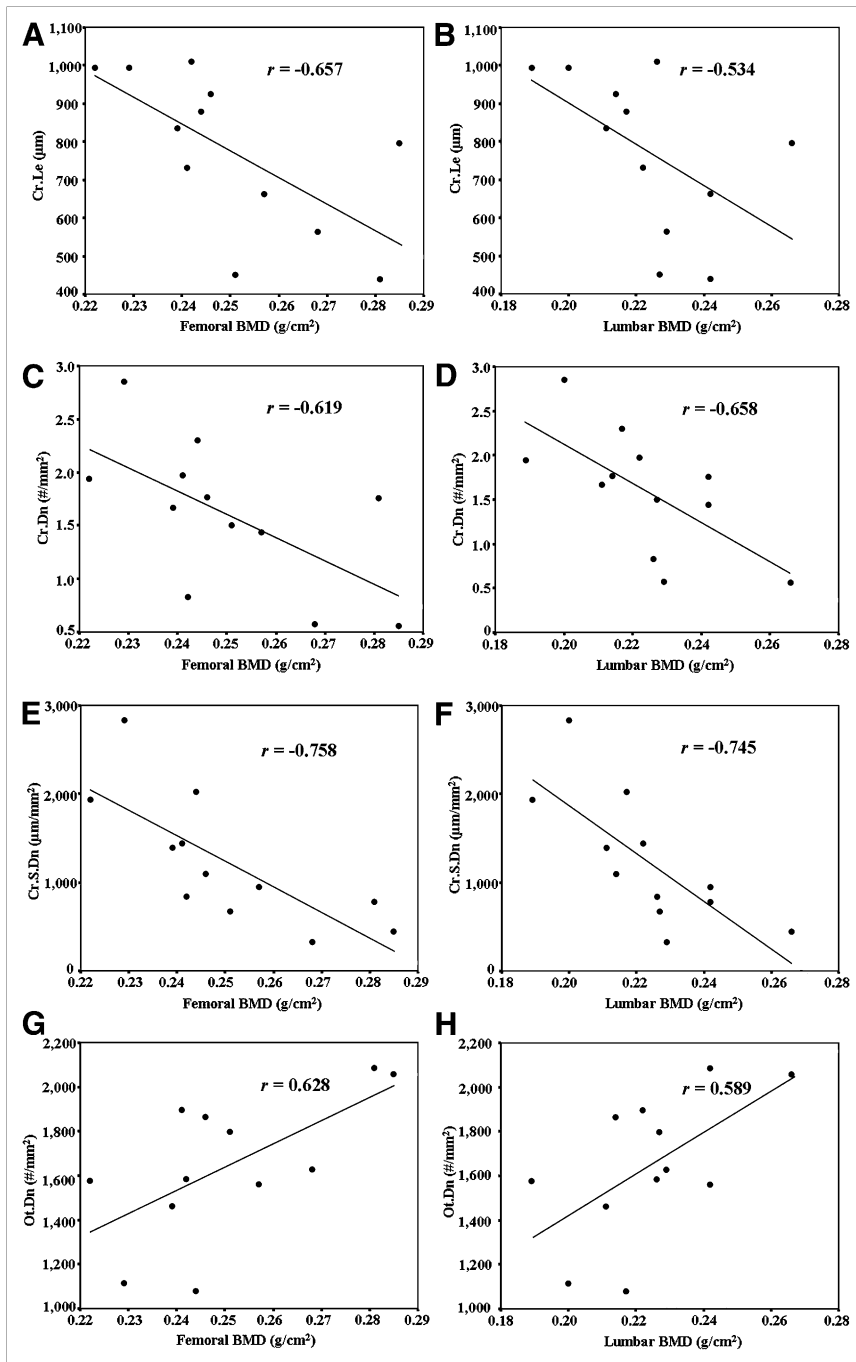


FIGURE 3. Correlation between BMD and microdamage histomorphology (Cr.Le, Cr.Dn, and Cr.S.Dn) and Ot.Dn in loaded limbs. (A) Correlation between femoral BMD and Cr.Le ($n = 12$, $P < 0.05$). (B) Correlation between lumbar BMD and Cr.Le ($n = 12$, $P > 0.05$). (C) Correlation between femoral BMD and Cr.Dn ($n = 12$, $P < 0.05$). (D) Correlation between lumbar BMD and Cr.Dn ($n = 12$, $P < 0.05$). (E) Correlation between femoral BMD and Cr.S.Dn ($n = 12$, $P < 0.05$). (F) Correlation between lumbar BMD and Cr.S.Dn ($n = 12$, $P < 0.05$). (G) Correlation between femoral BMD and Ot.Dn ($n = 12$, $P < 0.05$). (H) Correlation between lumbar BMD and Ot.Dn ($n = 12$, $P < 0.05$).

of a clinically relevant patient population with osteoporosis, Stepan et al. (27) found that microdamage accumulation correlated with low BMD and increased age, although these correlations were more apparent when compared with patients treated with bisphosphonates. However, further studies are required to delineate the clinical implication of bone microdamage evaluation in osteoporosis diagnosis and treatment.

There are some clinical studies in which osteoporotic patients were evaluated for bone metabolism changes in response to treatment by small-animal PET (28,29). To the

best of our knowledge, however, this is the first report of the use of small-animal PET/CT for skeletal microdamage evaluation in osteoporosis study. Our study showed that small-animal PET/CT can not only detect the microdamage in the tibial mid shafts caused by fatigue loading in rats but also locate microdamage in the skeleton of small animals accurately. Microdamage was noted in the tibial mid shafts after fatigue loading in rats of both groups, as shown by increased uptake of ¹⁸F-fluoride in the loaded tibial mid shafts on small-animal PET images, whereas no significant uptake was demonstrated in the control hind

limbs—consistent with the findings from microdamage histomorphology analysis, both in location and in magnitude.

The reasons underlying the success in detection and quantification of bone microdamage as shown by the increase in ^{18}F -fluoride uptake in the loaded bones might be explained by microdamage formation and subsequent increase in bone mineral surface (22,23,30,31), increased blood supply or interstitial fluid flow to the area of microdamage (23,32,33), and high bone turnover due to microdamage repair (34–36). There have been only 2 small-animal studies of PET of bone microdamage (22,23) confirming the sensitivity and specificity of PET. Li et al. (22) detected the newly created microdamage 1 d after fatigue loading, and enhanced accumulation of tracer was seen only on the loaded bones with microdamage. These authors suggested that PET can distinguish the increased blood flow associated with no microdamage from mechanically induced microdamage. Silva et al. (23) found that fluoride uptake in the central region of microdamage was increased in proportion to the severity of damage as defined by the magnitude of fatigue loading. Combined with our findings, high-resolution PET/CT may provide an effective noninvasive means to image bone microdamage in vivo.

The limitation to our study was that we did not assess the time course of bone microdamage as shown by PET intensity. We hope in further studies to observe the effect of osteoporosis on the repair and reconstruction process of microdamage at multiple time points, to demonstrate the relationship between bone microdamage and the biomechanical behavior of the whole bones. As expected, the cortical bone parameters did not differ significantly between ovariectomy and sham rats in this study. The pattern mechanism of load transmission along the bone needs to be clarified. Silva et al. (27) suggested that intracortical remodeling might be involved in the fluoride uptake after fatigue loading. Recently, a study by Kidd et al. (37) has provided evidence supporting the hypothesis that stress fractures heal by direct remodelling along the fracture line. Ex vivo autoradiography may be necessary to accurately delineate the ^{18}F -fluoride uptake and distribution in bone. Also, the biologic response of bone to microdamage in healthy or osteoporotic bone needs to be studied by demonstrating bone turnover change with regard to initiation, propagation, and repair of bone microdamage.

CONCLUSION

The tibial mid shafts of the ovariectomized rats showed more bone microdamage after fatigue loading than did those of the sham rats. These results suggested that osteoporosis due to estrogen deficiency may be associated with impairment of bone strength and, in turn, with increase in fracture risk. Small-animal PET/CT is a useful noninvasive means to detect and quantify bone microdamage in vivo. Moreover, it can also locate microdamage in the animal skeleton accurately.

DISCLOSURE STATEMENT

The costs of publication of this article were defrayed in part by the payment of page charges. Therefore, and solely to indicate this fact, this article is hereby marked “advertisement” in accordance with 18 USC section 1734.

ACKNOWLEDGMENT

This study was supported by the National Natural Science Foundation of China (U1032001).

REFERENCES

1. Turner CH. Biomechanics of bone: determinants of skeletal fragility and bone quality. *Osteoporos Int.* 2002;13:97–104.
2. Seeman E, Delmas PD. Bone quality: the material and structural basis of bone strength and fragility. *N Engl J Med.* 2006;354:2250–2261.
3. Burr DB, Forwood MR, Fyhrie DP, Martin RB, Schaffler MB, Turner CH. Bone microdamage and skeletal fragility in osteoporotic and stress fractures. *J Bone Miner Res.* 1997;12:6–15.
4. Burr D. Microdamage and bone strength. *Osteoporos Int.* 2003;14(suppl 5):S67–S72.
5. Chapurlat RD, Delmas PD. Bone microdamage: a clinical perspective. *Osteoporos Int.* 2009;20:1299–1308.
6. Schaffler MB. Role of bone turnover in microdamage. *Osteoporos Int.* 2003;14(suppl 5):S73–S80.
7. Donahue SW, Galley SA. Microdamage in bone: implications for fracture, repair, remodeling, and adaptation. *Crit Rev Biomed Eng.* 2006;34:215–271.
8. Cardoso L, Herman BC, Verborgt O, Laudier D, Majeska RJ, Schaffler MB. Osteocyte apoptosis controls activation of intracortical resorption in response to bone fatigue. *J Bone Miner Res.* 2009;24:597–605.
9. Mori S, Harruff R, Ambrosius W, Burr DB. Trabecular bone volume and microdamage accumulation in the femoral heads of women with and without femoral neck fractures. *Bone.* 1997;21:521–526.
10. Diab T, Condon KW, Burr DB, Vashishth D. Age-related change in the damage morphology of human cortical bone and its role in bone fragility. *Bone.* 2006;38:427–431.
11. Nagaraja S, Lin ASP, Guldberg RE. Age-related changes in trabecular bone microdamage initiation. *Bone.* 2007;40:973–980.
12. Hetzel M, Arslanagic C, König HH, et al. F-18 NaF PET for detection of bone metastases in lung cancer: accuracy, cost-effectiveness, and impact on patient management. *J Bone Miner Res.* 2003;18:2206–2214.
13. Even-Sapir E, Metser U, Flusser G, et al. Assessment of malignant skeletal disease: initial experience with ^{18}F -fluoride PET/CT and comparison between ^{18}F -fluoride PET and ^{18}F -fluoride PET/CT. *J Nucl Med.* 2004;45:272–278.
14. Dasa V, Adbel-Nabi H, Anders MJ, Mihalko WM. F-18 fluoride positron emission tomography of the hip for osteonecrosis. *Clin Orthop Relat Res.* 2008;466:1081–1086.
15. De Souza RL, Matsuura M, Eckstein F, Rawlinson SC, Lanyon LE, Pitsillides AA. Non-invasive axial loading of mouse tibiae increases cortical bone formation and modifies trabecular organization: a new model to study cortical and cancellous compartments in a single loaded element. *Bone.* 2005;37:810–818.
16. *Guide for the Care and Use of Laboratory Animals.* Washington, DC: National Academy Press; 1996.
17. Sugiyama T, Saxon LK, Zaman G, et al. Mechanical loading enhances the anabolic effects of intermittent parathyroid hormone (1-34) on trabecular and cortical bone in mice. *Bone.* 2008;43:238–248.
18. Moustafa A, Sugiyama T, Saxon LK, et al. The mouse fibula as a suitable bone for the study of functional adaptation to mechanical loading. *Bone.* 2009;44:930–935.
19. Wohl GR, Towler DA, Silva MJ. Stress fracture healing: fatigue loading of the rat ulna induces upregulation in expression of osteogenic and angiogenic genes that mimic the intramembranous portion of fracture repair. *Bone.* 2009;44:320–330.
20. Griffin MG, Kimble R, Hopfer W, Pacifici R. Dual-energy x-ray absorptiometry of the rat: accuracy, precision, and measurement of bone loss. *J Bone Miner Res.* 1993;8:795–800.
21. Parfitt AM, Drezner MK, Glorieux FH, et al. Bone histomorphometry: standardization of nomenclature, symbols, and units—report of the ASBMR Histomorphometry Nomenclature Committee. *J Bone Miner Res.* 1987;2:595–610.

22. Li J, Miller MA, Hutchins GD, Burr DB. Imaging bone microdamage in vivo with positron emission tomography. *Bone*. 2005;37:819–824.
23. Silva MJ, Uthgenannt BA, Rutlin JR, Wohl GR, Lewis JS, Welch MJ. In vivo skeletal imaging of ¹⁸F-fluoride with positron emission tomography reveals damage- and time-dependent responses to fatigue loading in the rat ulna. *Bone*. 2006;39:229–236.
24. Burr DB, Hooser M. Alterations to the en bloc basic fuchsin staining protocol for the demonstration of microdamage produced in vivo. *Bone*. 1995;17:431–433.
25. Danova NA, Colopy SA, Radtke CL, et al. Degradation of bone structural properties by accumulation and coalescence of microcracks. *Bone*. 2003;33:197–205.
26. Dai RC, Liao EY, Yang C, Wu XP, Jiang Y. Microcracks: an alternative index for evaluating bone biomechanical quality. *J Bone Miner Metab*. 2004;22:215–223.
27. Stepan JJ, Burr DB, Pavo I, et al. Low bone mineral density is associated with bone microdamage accumulation in postmenopausal women with osteoporosis. *Bone*. 2007;41:378–385.
28. Frost ML, Blake GM, Park-Holohan SJ, et al. Long-term precision of ¹⁸F-fluoride PET skeletal kinetic studies in the assessment of bone metabolism. *J Nucl Med*. 2008;49:700–707.
29. Uchida K, Nakajima H, Miyazaki T, et al. Effects of alendronate on bone metabolism in glucocorticoid-induced osteoporosis measured by ¹⁸F-fluoride PET: a prospective study. *J Nucl Med*. 2009;50:1808–1814.
30. Hoh CK, Hawkins RA, Dahlbom M, et al. Whole body skeletal imaging with ¹⁸F-fluoride ion and PET. *J Comput Assist Tomogr*. 1993;17:34–41.
31. Langsteger W, Heinisch M, Fogelman I. The role of fluorodeoxyglucose, ¹⁸F-dihydroxyphenylalanine, ¹⁸F-choline, and ¹⁸F-fluoride in bone imaging with emphasis on prostate and breast. *Semin Nucl Med*. 2006;36:73–92.
32. Hsieh YF, Silva MJ. In vivo fatigue loading of the rat ulna induces both bone formation and resorption and leads to time-related changes in bone mechanical properties and density. *J Orthop Res*. 2002;20:764–771.
33. Matsuzaki H, Wohl GR, Novack DV, Lynch JA, Silva MJ. Damaging fatigue loading stimulates increases in periosteal vascularity at sites of bone formation in the rat ulna. *Calcif Tissue Int*. 2007;80:391–399.
34. Narita N, Kato K, Nakagaki H, Ohno N, Kameyama Y, Weatherell JA. Distribution of fluoride concentration in the rat's bone. *Calcif Tissue Int*. 1990;46:200–204.
35. Cook GJ, Lodge MA, Marsden PK, Dynes A, Fogelman I. Non-invasive assessment of skeletal kinetics using fluorine-18 fluoride positron emission tomography: evaluation of image and population-derived arterial input functions. *Eur J Nucl Med*. 1999;26:1424–1429.
36. Verborgt O, Gibson GJ, Schaffler MB. Loss of osteocyte integrity in association with microdamage and bone remodeling after fatigue in vivo. *J Bone Miner Res*. 2000;15:60–67.
37. Kidd LJ, Stephens AS, Kuliwaba JS, Fazzalari NL, Wu ACK, Forwood MR. Temporal pattern of gene expression and histology of stress fracture healing. *Bone*. 2010;46:369–378.